Exotic Resonant States for One-Dimensional Twin Complex Square Potentials

Cornelia Grama, Nicolae Grama, and Ioan Zamfirescu

Horia Hulubei National Institute for Physics and Nuclear Engineering, Bucharest, P.O. Box MG-6, Romania

Reprint requests to N. G.; E-mail: grama@theory.nipne.ro

Z. Naturforsch. **68a,** 587 – 598 (2013) / DOI: 10.5560/ZNA.2013-0049
Received February 12, 2013 / published online August 21, 2013

The natural modes for one-dimensional (1D) twin square potentials of complex strength g are studied. A global analysis of the natural modes based on the construction of the Riemann surfaces R_g^{I} and R_g^{II} of the multiple valued function $k = k(g)$, where $k(g)$ defines the poles of the transmission coefficient, is done. To each nonradiative or radiative mode a sheet of the Riemann surface is associated. All the natural modes of the system are identified and treated in a unified way. New classes of resonant state poles with exotic properties are identified on the k-plane images of the sheets of R_g^{I} and R_g^{II} and the properties of the exotic modes are studied. The traversal time through the 1D twin square potentials is analysed. Subluminal and superluminal traversal times are evidenced. An approximate formula for the frequencies k for which the maximal superluminal velocities are gained as a function of the potential parameters is given.

Key words: Tunnelling; Natural Modes; Traversal Time; Scattering Theory.

1. Introduction

Tunnelling is a fundamental process related to the dynamics of various kinds of waves and it is frequently encountered in physics. Tunnelling, described by the Schrödinger equation with a potential barrier higher than the particle's total energy, is allowed by quantum mechanics theory and is probably the most important physical process. There is a formal similarity between the stationary Schrödinger equation and the usual wave equation. As with quantum mechanics, solutions of wave equation lead to a discrete set of bound modes and a continuum of radiation modes. Photonic barriers are produced in undersized wave guides, frustrated total internal reflection, or photonic lattice (periodic dielectric heterostructure). The optical tunnelling process has been studied in the range of frequencies from microwaves to ultraviolet (UV) region. A detailed overview of the entire field of optical tunnelling and its relation to massive-particle tunnelling is given in [1, 2].

A different, but related, issue is that of particle tunnelling through a double barrier potential structure. Exploiting the analogy between electron and photon tunnelling [2], resonant tunnelling phenomena through double barrier structures have been studied. Resonant tunnelling observed in [3] became an important tool for studying the properties of semiconductors, metals, and superconductors. Anderson localization, Mott hopping, Josephson effect, field emission, Coulomb blockade, and tunnelling chemical reactions are only several examples of phenomena where the resonant tunnelling is important. The development of nanotechnology and electronic devices based on resonant tunnelling (see e. g. [4, 5]) has made quantum-mechanical tunnelling in one dimension an area of interest in applied science. The theoretical approach in the studies concerning the tunnelling is the analysis of the transmission coefficient. In the 1D problem, the transmission coefficient T manifests in its variation as a function of energy the existence of resonant states. The resonant and bound states are the radiative and nonradiative natural modes, respectively, of the quantum system. The natural modes are intrinsic distinctive marks of the system, that characterize the system like a fingerprint. The studies on the double barrier potentials [6 – 8] are nonglobal. In the present paper, we give a global analysis of the natural modes, based on the

Riemann surface approach, that allows the simultaneous treatment of the cases of two wells or two barriers, with absorption or emission, and gives an unitary treatment to bound and resonant states. In other words, we analyze all the natural modes of the system. All the poles of the transmission coefficient are identified, no pole is lost, no accidental jump (as it happens in the pole trajectory method) from one pole to another pole is possible. Whenever the Riemann surface approach was used for a three-dimensional (3D) potential, new information on the resonant states has been obtained [9–11]. A new class of resonant state poles (exotic poles), having unusual properties, has been identified for a 3D potential made of a well plus a barrier. In the case of a 3D potential made of a well plus a Coulomb barrier [10], it has been shown that the di-nuclear parent quasimolecular states are a particular case of exotic resonant states for this potential. All the properties of the di-nuclear parent quasimolecular states result in a natural way from the properties of the exotic resonant states.

The renewed interest in the study of the tunnel effect occurred mainly due to the data on the traversal time in tunnelling. A comparison of numerical traversal times [12] for a narrow and for a thick barrier to the semi-classical time [13], to the phase-time [14], and to the dwell time [15, 16] results shows that the best overall description is given by the phase-time result. In the present paper, the traversal time for the twin square potentials model will be determined by the phase-shift method. It will be shown that a faster traversal in comparison with that of a free particle is possible. It is not a surprising result, as the experiments revealed superluminal (faster than light) velocities. Experimentally it has been shown that the traversal time is independent of the barrier length [17], as Hartmann [18] has predicted fifty years ago. New experimental and theoretical data on superluminal tunnelling could be found in [19]. The problem of superluminal velocity is not only of academic interest, but a problem of technology development too. For example, the superluminal ring laser gyroscope first proposed by Yum et al. [20] improves the sensitivity of a gyroscope by a factor 10^3–10^6 and can be used for improving the sensitivity of accelerometers by the same factor. This technology can be used for application to precision navigation, precision measurement of vibration, strain and magnetic field, and gravitational wave detectors.

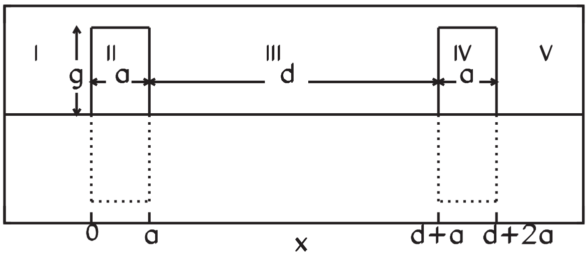

Fig. 1. Parameters of the potential.

2. Tunnelling Through One-Dimensional Twin Complex Square Potentials

Let us consider the one-dimensional potential $gV(x)$, $g \in \mathbb{C}$, represented in Figure 1: g is the strength, and $V(x)$ is the form-factor with the values $V(x) = 0$ in the regions $x \leq 0$, $a < x < a+d$, and $x > d+2a$, while in the regions $0 < x \leq a$ and $a+d < x < d+2a$, we have $V(x) = -1$. This represents twin square barriers ($\mathrm{Re}(g) < 0$), or twin square wells ($\mathrm{Re}(g) > 0$) potentials with an absorptive ($\mathrm{Im}(g) > 0$) or emissive part ($\mathrm{Im}(g) < 0$), having equal strength for the two barriers (wells). a is the width of the potential wells (barriers), d is the distance between the two wells (barriers). For the sake of simplicity, the notation k and g is used for the dimensionless variables ka and ga^2, respectively. By I, III, and V the regions of the free wave are denoted. The wave function in the regions denoted by I, II, III, IV, and V are

$$\begin{aligned}
&\psi_I = \mathrm{e}^{\mathrm{i}kx} + R\,\mathrm{e}^{-\mathrm{i}kx}, \quad \psi_{\mathrm{II}} = C_1\,\mathrm{e}^{\mathrm{i}k_0x} + C_2\,\mathrm{e}^{-\mathrm{i}k_0x}, \\
&\psi_{\mathrm{III}} = C_3\,\mathrm{e}^{\mathrm{i}kx} + C_4\,\mathrm{e}^{-\mathrm{i}kx}, \\
&\psi_{\mathrm{IV}} = C_5\,\mathrm{e}^{\mathrm{i}k_0x} + C_6\,\mathrm{e}^{-\mathrm{i}k_0x}, \quad \psi_{\mathrm{V}} = T\,\mathrm{e}^{\mathrm{i}kx},
\end{aligned} \tag{1}$$

where $k_0 = (k^2+g)^{1/2}$. The coefficients $R, C_1, C_2, \ldots, C_6$, and T can be determined by imposing the condition of continuity to the wave function, i. e. by imposing that $\psi_I = \psi_{\mathrm{II}}$ and $\mathrm{d}\psi_I/\mathrm{d}x = \mathrm{d}\psi_{\mathrm{II}}/\mathrm{d}x$ at $x = 0$, $\psi_{\mathrm{II}} = \psi_{\mathrm{III}}$ and $\mathrm{d}\psi_{\mathrm{II}}/\mathrm{d}x = \mathrm{d}\psi_{\mathrm{III}}/\mathrm{d}x$ at $x = a$, and so on. The amplitude of the incident wave is considered unity, R is the amplitude of the reflected wave, and T is the amplitude of the transmitted wave. The poles of T are the S-matrix poles.

The transmission coefficient T can be written as

$$T = T_1/T_2 = \frac{16k_0^2k^2\,\mathrm{e}^{2\mathrm{i}k_0a}\,\mathrm{e}^{-2\mathrm{i}ka}}{(s_2-s_1)(s_2+s_1)}, \tag{2}$$

with $s_2 = (k-k_0)^2\,\mathrm{e}^{2\mathrm{i}k_0a} - (k+k_0)^2$ and $s_1 = (\mathrm{e}^{2\mathrm{i}k_0a} - 1)(k-k_0)(k_0+k)\,\mathrm{e}^{\mathrm{i}kd}$. As T_2 can be written as product of two terms, two families of S-matrix poles are obtained. They are the solutions of the equations

$$s_2 - s_1 = 0\,, \quad s_2 + s_1 = 0\,. \tag{3}$$

By using the relation $\cot x = \mathrm{i}(\mathrm{e}^{2\mathrm{i}x}+1)/(\mathrm{e}^{2\mathrm{i}x}-1)$ in (3), the following pole equations are obtained:

$$\cot(k_0a) + \frac{\mathrm{i}}{2kk_0}\left[-\,\mathrm{e}^{\mathrm{i}kd}(k_0^2-k^2) - k^2 - k_0^2\right] = 0\,, \tag{4}$$

$$\cot(k_0a) + \frac{\mathrm{i}}{2kk_0}\left[\mathrm{e}^{\mathrm{i}kd}(k_0^2-k^2) - k^2 - k_0^2\right] = 0\,. \tag{5}$$

In order to construct the Riemann surface of the pole function $k = k(g)$ for the twin complex square potentials, the knowledge of the branch points is necessary.

3. Branch Points

3.1. Algebraic Branch Points

The singular points are solutions of the system of equations made of the pole equation and of its derivative with respect to k. In the case of the potential represented in Figure 1, there are two pole equations (4) and (5). Correspondingly there are two equations representing the derivatives with respect to k of the pole equations The equations obtained by eliminating $\cot(k_0a)$ between (4) and its derivative with respect to k, and between (5) and its derivative with respect to k, respectively, are even-functions with respect to k_0. By introducing k_0^2 obtained by solving these equations in (4) and (5), respectively, the equations that give the k-plane images $\kappa_{\mu,\nu}^{p,q}$ of the singular points are obtained:

$$\cos(kaA) + \mathrm{i}\,\frac{U-Z}{(V+Y)A}\,\sin(kaA) = 0\,, \tag{6}$$

$$\cos(kaB) + \mathrm{i}\,\frac{U-S}{(V-Y)B}\,\sin(kaB) = 0\,. \tag{7}$$

where the following notations are used: $S = 2\mathrm{i} + ka - kd\mathrm{e}^{\mathrm{i}kd}$, $U = (2\mathrm{i}+ka+kd)\,\mathrm{e}^{2\mathrm{i}kd}$, $V = 2\mathrm{i}+ka+ka\mathrm{e}^{2\mathrm{i}kd}$, $X = (2\mathrm{i}+2ka)\,\mathrm{e}^{\mathrm{i}kd}$, $Y = (2\mathrm{i}+2ka+2kd)\,\mathrm{e}^{\mathrm{i}kd}$, $Z = 2\mathrm{i}+ka+kd\,\mathrm{e}^{\mathrm{i}kd}$, $A = ((-X+V)/(Y+V))^{1/2}$, $B = ((X+V)/(-Y+V))^{1/2}$.

Once the solutions k are determined from (6) and (7), respectively, the corresponding g are determined by solving (4) and (5), respectively. Among these singular points g_i, the branch points are found by permitting the variable g to describe successive small circles around each singular point g_i and observing whether the function $k = k(g)$ returns to its initial value. Being zeros of a system of analytical functions, the branch points form at most a countable infinite set.

New quantum numbers p, q, μ, and ν are necessary in order to label the branch points. In order to understand their meaning, in Figure 2 the k-plane images $\kappa_{\mu,\nu}^{p,q}$ of the branch points are shown. The label $p = \mathrm{I},\mathrm{II}$ indicates the set of equations that has $\kappa_{\mu,\nu}^{p,q}$ as solution. $\kappa_{\mu,\nu}^{\mathrm{I},q}$ are obtained as solutions of (6), while $\kappa_{\mu,\nu}^{\mathrm{II},q}$ are obtained as solutions of (7). The k-plane images of the branch points are distributed along two distinct curves labeled by $q = 1$ and $q = 2$, respectively. The k-plane images of the branch points with the same value for the labels p and q are clustered in groups, each of the groups being labeled by the quantum number μ. By ν the various branch points with the same p, q, and μ are labeled. These branch points are characterized by the same position in the k-plane, but different values of the potential strength as one can see from Figure 3.

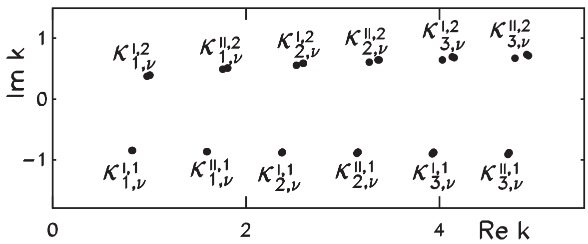

Fig. 2. k-plane images $\kappa_{\mu,\nu}^{p,q}$ of the branch points with $\mathrm{Im}(\kappa) < 5$ for $a = 0.25$, $d = 4$.

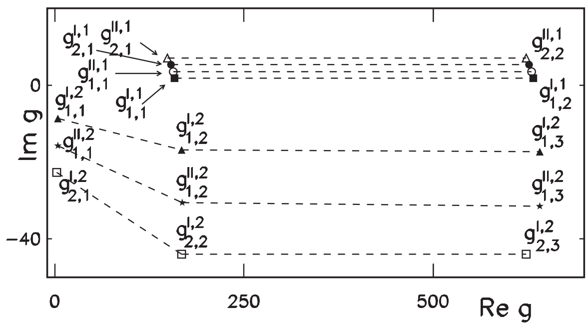

Fig. 3. Branch points $g_{\mu,\nu}^{p,q}$ with $\mathrm{Re}(g_{\mu,\nu}^{p,q}) < 650$ and $-40 < \mathrm{Im}(g_{\mu,\nu}^{p,q}) < 8$ for $a = 0.25$, $d = 4$. The quantum numbers p, q, μ, and ν have the same meaning as in Figure 2.

3.1.1. Asymptotic Approximation for the k-Plane Images of the Algebraic Branch Points

In the exact numerical calculation of the branch points, (6) and (7) have to be solved, and it is important to have a good starting point for k. Consequently approximate values for the k-plane images of the algebraic branch points are necessary. In order to get these approximate values, only the main term for large k_0 (i. e. for large g) has been kept in the equations obtained by eliminating $\cot k_0 a$ between (4) and its derivative with respect to k, and between (5) and its derivative with respect to k, respectively. Two second-degree equations in respect to $\exp(\mathrm{i}kd)$ are obtained. To distinguish between these two equations, the label $p = \mathrm{I}, \mathrm{II}$ will be used:

$$ak\mathrm{e}^{2\mathrm{i}kd} \pm (2kd + 2\mathrm{i} + 2ak)\,\mathrm{e}^{\mathrm{i}kd} + 2\mathrm{i} + ka = 0\,. \qquad (8)$$

Each of the equations (8) has two solutions with respect to k, labeled by $q = 1, 2$. Asymptotic expansions of the two solutions of each of (8) for large d have been taken and solved with respect to k. The obtained approximate expressions of the algebraic branch points for large d and g are

$$\kappa_n^{p,q} \sim -\frac{\mathrm{i}}{d}\left\{\ln\left[\mp\frac{2}{a}(d+a)\right] + 2\mathrm{i}(n-2+q)\pi\right\}, \qquad (9)$$
$$n = 1, 2, 3, \ldots$$

$$\kappa_n^{p,q} \sim -\frac{\mathrm{i}}{d}\mathrm{Lambert\,W}\left(n, \pm 1 \mp \frac{a}{2d}\mathrm{Lambert\,W}(n, \pm 1)\right),$$
$$n = 1, 2, 3, \ldots \qquad (10)$$

Table 1. First complex algebraic branch points $g_{\mu,\nu}^{p,q}$ and their k-plane images $\kappa_{\mu,\nu}^{p,q}$ ($\mu = 1, 2$ and $\nu = 1, 2$) for $a = 0.25$ and $d = 4$.

p	q	μ	ν	$\mathrm{Re}(g_{\mu,\nu}^{p,q})$	$\mathrm{Im}(g_{\mu,\nu}^{p,q})$	$\mathrm{Re}(\kappa_{\mu,\nu}^{p,q})$	$\mathrm{Im}(\kappa_{\mu,\nu}^{p,q})$
I	1	1	1	158.496	1.769	0.822	−0.847
I	1	1	2	632.235	1.774	0.823	−0.847
I	2	1	1	4.449	−8.636	0.979	0.372
I	2	1	2	167.626	−16.879	1.008	0.391
I	1	2	1	153.617	5.321	2.372	−0.883
I	1	2	2	627.319	5.307	2.376	−0.876
I	2	2	1	2.343	−22.743	2.521	0.556
I	2	2	2	167.487	−43.939	2.591	0.591
II	1	1	1	156.669	3.536	1.596	−0.871
II	1	1	2	630.394	3.538	1.599	−0.868
II	2	1	1	3.978	−15.755	1.759	0.485
II	2	1	2	168.272	−30.549	1.810	0.512
II	1	2	1	149.346	7.135	3.150	−0.893
II	1	2	2	623.012	7.084	3.156	−0.881
II	2	2	1	−0.277	−29.641	3.277	0.606
II	2	2	2	165.632	−57.203	3.366	0.649

Table 2. First three real algebraic branch points g_n^{I} and g_n^{II} and their k-plane images for $a = 0.25$, $d = 4$.

n	g_n^{I}	κ_n^{I}	n	g_n^{II}	κ_n^{II}
1	156.8882	−0.28271i	1	159.0947	−0.79737i
2	630.6305	−0.28275i	2	632.6405	−0.79802i
3	1420.1991	−0.28276i	3	1422.4066	−0.79895i

The Lambert W function satisfies the equation $\mathrm{Lambert\,W}(x)\exp(\mathrm{Lambert\,W}(x)) = x$ [21]. As the equation $y(x)\exp(y(x)) = x$ has an infinite number of solutions y for each (nonzero) value of x, Lambert W has an infinite number of branches denoted $\mathrm{Lambert\,W}(n, x)$, where n is any nonzero integer. The label n is the same as μ for the exact k-plane images $\kappa_{\mu,\nu}^{p,q}$ of the branch points. With $\kappa_n^{p,q}$ as starting points, exact numerically calculated k-plane images of the algebraic branch points $\kappa_{\mu,\nu}^{p,q}$ are obtained from (6) and (7), and then the corresponding branch points $g_{\mu,\nu}^{p,q}$ are calculated from (4) and (5). In Table 1 the first complex algebraic branch points $g_{\mu,\nu}^{p,q}$ are given in the case $a = 0.25$ and $d = 4$.

Besides the complex algebraic branch points there are real algebraic branch points, listed in Table 2, whose images are situated on the negative imaginary k-axis.

3.2. Transcendental Branch Points

Besides the algebraic branch points there is a transcendental branch point, namely $g = 0$, where all the Riemann sheets are joined. As the k-plane images of this branch point are the starting points in constructing the k-plane images of Riemann sheets, it is important to find approximate values for the k-plane images of the transcendental branch point. By taking a two terms expansion for small g in the pole equations (4) and (5), the following two equations are obtained:

Table 3. k-plane images of transcendental branch points with $\mathrm{Re}(\kappa_{p,n}) < 5.5$ for the values of the parameters $a = 0.25$ and $d = 4$.

p	m	s	n	$\mathrm{Re}(\kappa_{p,n})$	$\mathrm{Im}(\kappa_{p,n})$
I	1	2	1	0.7911	−2.8964
I	1	1	2	2.3416	−2.9600
I	2	2	3	3.8498	−3.0415
I	2	1	4	5.3331	−3.1256
II	1	1	1	1.5725	−2.9236
II	2	2	2	3.0999	−3.0001
II	2	1	3	4.5932	−3.0834

$$e^{2ika} = \frac{4k^2}{g} e^{-ikd}, \quad e^{2ika} = -\frac{4k^2}{g} e^{-ikd}. \qquad (11)$$

Each of the equations (11) has two solutions with respect to k. The solutions of (11) have a label $p = \mathrm{I}, \mathrm{II}$ to indicate the equation and a label $s = 1, 2$ in order to distinguish between the two solutions of each equation:

$$\kappa_{p,m,s} \sim \frac{2\mathrm{i}\,\mathrm{LambertW}\left(-m, \frac{(-1)^s \mathrm{i}^t}{4} g^{1/2}(2a+d)\right)}{(2a+d)}, \quad m = 1, 2, \ldots, \qquad (12)$$

where $t = 1$ for $p = \mathrm{I}$ and $t = 2$ for $p = \mathrm{II}$. The values of $\kappa_{p,m,s}$ given by (12) are used as starting points for the calculations of the exact values of the transcendental branch points. In the following, for practical reasons, we will drop the labels m, s and use for κ two labels: $p = \mathrm{I}, \mathrm{II}$ (that indicates the Riemann surface) and $n = 1, 2\ldots$ that orders the k-plane images of $g \to 0$ with respect to their distance to the imaginary k-axis (see Tab. 3).

4. Riemann Surfaces of the Pole Function $k(g)$

In the case studied in the present paper, there are two families of S-matrix poles, solutions of (4) and (5), respectively, corresponding to the zeros of each factor occurring in the denominator $T_2(g,k)$ of the function $T(g,k)$ (see (2)). We will write

$$T_2(g,k) = t^{(1)}(g,k)t^{(2)}(g,k), \qquad (13)$$

where $t^{(1)}(g,k) = s_2 - s_1$, and $t^{(2)}(g,k) = s_2 + s_1$. The functions $t^{(1)}(g,k)$ and $t^{(2)}(g,k)$ are entire functions with respect to g and k and they are irreducible. Each of the relations $t^{(1)}(g,k) = 0$ and $t^{(2)}(g,k) = 0$ defines the implicit function $k = k(g)$ which is a multivalued function. Due to the fact that the equation $t^{(1)}(g,k)\, t^{(2)}(g,k) = 0$ that defines the pole function $k = k(g)$ is reducible, the analytic manifold $\mathcal{R}_g$ on which the function $k = k(g)$ is single valued and analytic is made of two Riemann surfaces R_g^p ($p = \mathrm{I}, \mathrm{II}$). This means that $t^{(1)}(g,k) = 0$ defines the function $k = k(g)$ on the Riemann surface R_g^{I}, while $t^{(2)}(g,k) = 0$ defines the function $k = k(g)$ on the Riemann surface R_g^{II}. The function $k = k(g)$ becomes single valued and analytic when defined on Riemann surfaces R_g^{I} and R_g^{II}. In order to construct the Riemann surfaces R_g^{I} and R_g^{II} of the pole function $k = k(g)$ for the studied potential, the general properties of an implicit function $k(g)$ defined by an irreducible relation $\mathcal{F}(g,k) = 0$, where $\mathcal{F}(g,k)$ is an entire function with respect to k and g, will be used. These properties have been studied by Julia [22] and Stoilow [23, 24] and in the present case they are applied to the irreducible functions $t^{(1)}(g,k)$ and $t^{(2)}(g,k)$. Taking into account the expressions of the functions $T_1(g,k)$, $t^{(1)}(g,k)$, and $t^{(2)}(g,k)$ given by (2) and (3), respectively, it results that at $g = 0$ (i. e. $k_0 = k$), we have $T_1(g,k) = -16k^4$, $t^{(1)}(g,k) = t^{(2)}(g,k) = -4k^2$. It results that $t^{(1)}(g,k) = 0$ and $t^{(2)}(g,k) = 0$ have no solution at $g = 0$, except $k = 0$, but $k = 0$ is also solution for the numerator of $T(g,k)$. Then the boundary set E (the points g for which the equation $\mathcal{F}(g,k) = 0$ has no solution in k) has only one element, namely $g = 0$.

In order to illustrate the construction of the Riemann surfaces R_g^{I} and R_g^{II}, some particular values for a and d have been chosen, namely $a = 0.25$ and, $d = 4$. It is not possible to take into account all the branch points, nor their k-plane images. Indeed, there is an infinity of k-plane images of the branch points $\kappa_{\mu,\nu}^{p,q}$, and their distance from the imaginary k-axis increases indefinitely as μ increases, as it can be seen from Figure 2. Correspondingly, both the real part and the imaginary part of the branch points $g_{\mu,\nu}^{p,q}$ increases indefinitely as μ or ν increase (see Fig. 3). Consequently we can consider only a part of each Riemann surface, choosing a large radius circle in the g-plane ($|g| = 650$) and taking into account only the branch points that are situated inside the chosen circle. In fact this corresponds to the physical situation because the strength of the potential barriers (wells) is supposed to be finite. Moreover, the k-plane images of the branch points should be situated in a finite region of the k-plane. In Table 1 the first algebraic branch points $g_{\mu,\nu}^{p,q}$ ($\mu = 1, 2$), ($\nu = 1, 2$) are given. They are the branch points that determine the separation of the first sheets of the Riemann surfaces R_g^{I} and R_g^{II}. For a given Riemann surface the construction of each Riemann sheet starts at $g = 0$. At $g = 0$, there is an infinity of sheets that are joined. By permitting the variable g to describe successive small circuits round $g = 0$, starting from $g = 0 + \mathrm{i}\varepsilon$, the corresponding starting point in the description of each of the k-plane image is obtained. The labelling of the Riemann sheets and of their k-plane images is done by two quantum numbers. The first one is $p = \mathrm{I}, \mathrm{II}$ that indicates the Riemann surface. The second quantum number $n = 1,2,\ldots$ is the label of images $\kappa_{p,n}$ of the transcendental branch point $g = 0$ that orders them according to their distance from the imaginary k-axis. The k-plane image of $g = 0$ which is the closest to the imaginary k-axis takes the label $n = 1$, the next takes the label $n = 2$, and so on. The procedure is identical for both Riemann surfaces R_g^{I} and R_g^{II}.

The border of a sheet is made by the edges of the cuts that start at the transcendental branch point $g = 0$ and at those branch points that are branch points for the sheet under discussion, and by a circle of large radius joining the cuts. In order to determine which of the branch points $g_{\mu,\nu}^{p,q}$ are branch points on each particular Riemann sheet, successive small circuits have been taken round the given branch point. If after a complete rotation the pole reaches the same value as the initial value, than $g_{\mu,\nu}^{p,q}$ is not a branch point on the chosen Riemann sheet. If the pole reaches after a complete rotation a value that is different from the initial one, than $g_{\mu,\nu}^{p,q}$ is a branch point on the chosen Riemann sheet, and this sheet is joined at $g_{\mu,\nu}^{p,q}$ to another Riemann sheet. In order to separate the sheet, a cut starting from $g_{\mu,\nu}^{p,q}$ must be taken on the Riemann sheet under discussion. Once the branch points are determined, cuts are taken in the g-plane that join them, so that to separate the Riemann sheets.

The Riemann sheets $\Sigma_{\mathrm{I},n}$ and their k-plane images $\Sigma'_{\mathrm{I},n}$ with $n = 1,2$ are shown in Figure 4. When g goes along the border of the Riemann sheet $\Sigma_{\mathrm{I},n}$, the corresponding k describes the border of the k-plane image of the Riemann sheet $\Sigma'_{\mathrm{I},n}$. The borders of the sheets are shown in Figures 4a and d. The k-plane images of the sheet-borders are shown in Figures 4b and e. The hatched regions of $\Sigma_{\mathrm{I},n}$ ($n = 1,2$) on Figures 4a and d are mapped by the function $k = k(g)$ into the bound regions of the k-plane images $\Sigma'_{\mathrm{I},n}$ marked by the same hatching. In Figures 4c and f, the regions of the k-plane where the bound regions marked by hatching on Figures 4b and e are situated, are represented at an enlarged scale. The label n is determined by the k-plane image of the pole for $g \to 0$, as explained above.

On the sheet $\Sigma_{\mathrm{I},1}$, there are three cuts that start at $g = 0$, $g_{1,1}^{\mathrm{I},1}$ and $g_{1,1}^{\mathrm{I},2}$ (denoted by a, d, and s on Fig. 4a). For $g \to 0$, the corresponding pole is situated at $\kappa_{\mathrm{I},1}$ given in Table 3 and indicated by A on Figure 4b. All the points of $\Sigma_{\mathrm{I},1}$ with $\mathrm{Im}\,g > \mathrm{Im}(g_{1,\nu}^{\mathrm{I},1})$ are mapped onto a bound region of $\Sigma'_{\mathrm{I},1}$ situated in the fourth quadrant of the k-plane and marked by hatching. Moreover, all the points of $\Sigma_{\mathrm{I},1}$ with negative $\mathrm{Im}(g)$ and $|\mathrm{Im}(g)| > |\mathrm{Im}(g_{1,\nu}^{\mathrm{I},2})|$ are mapped onto a bound region of $\Sigma'_{\mathrm{I},1}$ situated in the first quadrant of the k-plane. Poles situated inside the hatched regions have special properties that will be discussed in the next section.

On the sheet $\Sigma_{\mathrm{I},2}$, there are five cuts determined by the branch points $g = 0$, $g_{1,1}^{\mathrm{I},1}$, $g_{2,1}^{\mathrm{I},1}$, $g_{1,1}^{\mathrm{I},2}$, and $g_{2,1}^{\mathrm{I},2}$. All

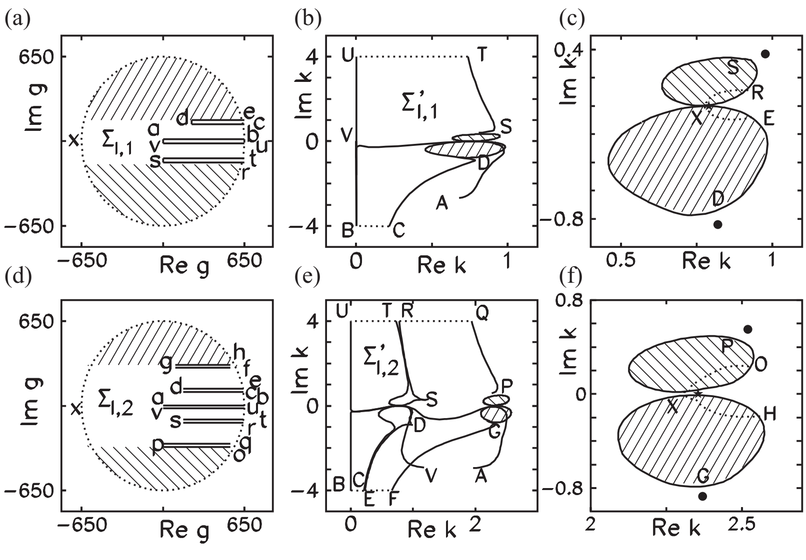

Fig. 4. Riemann sheets $\Sigma_{\mathrm{I},n}$ and their k-plane images $\Sigma'_{\mathrm{I},n}$ with $n = 1,2$.

the points of $\Sigma_{\mathrm{I},2}$ with $\mathrm{Im}(g) > \mathrm{Im}(g_{2,\nu}^{\mathrm{I},1})$ are mapped onto a bound region of $\Sigma'_{\mathrm{I},2}$ situated in the fourth quadrant of the k-plane. Moreover, all the points of $\Sigma_{\mathrm{I},2}$ with $|\mathrm{Im}(g)| > |\mathrm{Im}(g_{2,\nu}^{\mathrm{I},2})|$ are mapped onto a bound region of $\Sigma'_{\mathrm{I},2}$ situated in the first quadrant of the k-plane.

The situation is similar for the Riemann surface R_g^{II}, with the difference that the cuts on the Riemann sheets are determined by the branch points with the label $p = II$ in Tables 1, 2, and Table 3 and the positions of the bound regions on the k-plane images $\Sigma'_{\mathrm{II},n}$ are different.

5. New Class of Resonant Poles (Exotic Poles)

It has been shown that on each of the Riemann sheets, for both Riemann surfaces R_g^{I} and R_g^{II}, there are large regions that are mapped by the function $k = k(g)$ onto small bound regions of the corresponding k-plane images of the sheets. In other words, by varying the potential strength g in a large domain in the complex plane, the corresponding pole remains inside this bound region. This pole and the corresponding resonant state have unusual properties, and we will call them 'exotic resonant state pole' and 'exotic resonant state', respectively. An exotic resonant state pole does not become bound or virtual state pole if the depth of the wells is increased, in contrast to the old-class poles. On each k-plane image $\Sigma'_{p,n}$, there are two bound regions, one corresponding to absorptive potentials, the other to emissive potentials, where the exotic resonant state poles are located. The region of the k-plane that is occupied by the exotic poles on $\Sigma'_{p,n}$ is empty on the other Riemann sheet images $\Sigma'_{p,m}$ $(m \neq n)$ of the same Riemann surface.

In Figure 5, the aggregate obtained by superposing the sheet images $\Sigma'_{p,n}$, with $p = \mathrm{I}, \mathrm{II}$ and $n = 1, 2, 3$, is shown in the case $d = 4$, $a = 0.25$. Only the bound regions of the exotic poles are represented. Each bound

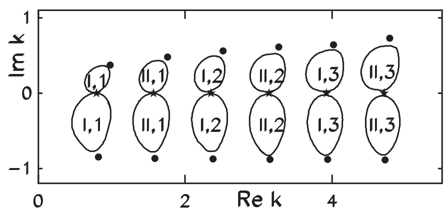

Fig. 5. Bound regions in the k-plane where 'exotic' poles are situated. The labels of the Riemann sheet images on which these bound regions occur are indicated. By • and $\star$, the branch point images and the attractors, respectively, are indicated.

region lies on a pair of points: a branch point image and a point that we call 'attractor' (or stable point) for the reason shown in the following. We denote the attractor point by $\mathcal{K}_n^p$, where n and p are the labels of the Riemann sheet image $\Sigma'_{p,n}$ to which belongs the attractor. The way the exotic resonant state pole on $\Sigma'_{\mathrm{II},2}$ approaches the attractor is illustrated in Figure 6a for $d = 4$, $a = 0.25$. The shown trajectory corresponds to g varying as $g = \lambda(20 + \mathrm{i})$, where λ takes values in the range 7 – 150. The domain of variation for g in Figure 6a is chosen so that the strength of the potential well $|g|$ increases inside the region characterized by $\mathrm{Im}(g) > \mathrm{Im}(g_{2,\nu}^{\mathrm{II},1})$. The corresponding pole is an exotic resonant state pole. One can see that the pole has a spiral trajectory that shrinks towards the attractor as the strength of the potential wells increases. In Figure 6b, the pole trajectories on $\Sigma'_{\mathrm{II},2}$ obtained when g goes in the g-plane along paths with constant $\mathrm{Im}(g)$ for various values of $\mathrm{Im}(g)$ are shown. $\mathrm{Re}(g)$ varies from 150 to -400, i. e. one passes from a well of decreasing depth to a higher and higher barrier. It is shown that if g varies along a path with constant $\mathrm{Im}(g)$, the trajectories of the old-class poles are convergent to the attractor when the strength of the barrier increases, even though $\mathrm{Im}(g) < \mathrm{Im}(g_{2,\nu}^{\mathrm{II},1})$. In other words, an old-class pole coming from outside the bound region goes to the attractor when the strength of the potential barriers increases.

Asymptotic approximations for large g of the attractors have been obtained taking into account that at the attractor, we have $\mathrm{d}k/\mathrm{d}g \to 0$ for $g \to \infty$. By expanding the derivatives with respect to g of (4) and (5) for large g and by solving the obtained equations with respect to k, the following asymptotic approximations for the attractors on the k-plane sheet images of the Riemann surfaces R_g^{I} and R_g^{II}, respectively, result:

$$\mathcal{K}_n^{\mathrm{I}} \sim (2n-1)\pi/d\,, \quad \mathcal{K}_n^{\mathrm{II}} \sim 2n\pi/d\,, \quad n = 1, 2 \ldots \qquad (14)$$

The attractors are situated on the real k-axis. The resonant states (radiative modes) corresponding to poles in the neighbourhood of the attractors have energies that are almost real. It results from (14) that for both Riemann surfaces R_g^p, $(p = \mathrm{I}, \mathrm{II})$ the distance between the attractors on two successive Riemann sheet images $\Sigma'_{p,n}$ and $\Sigma'_{p,n+1}$ is $2\pi/d$, so that the attractors on various sheet images of a Riemann surface become more dense as the distance d between the

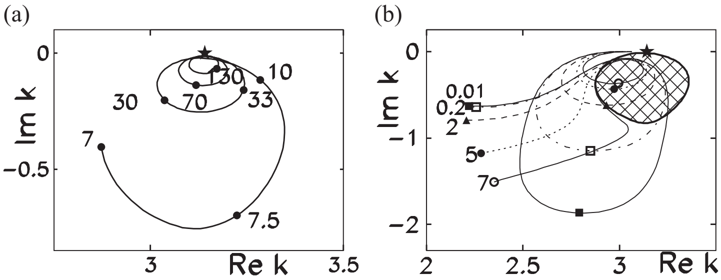

Fig. 6. (a) Trajectory of the pole on $\Sigma'_{\mathrm{II},2}$ for g varying as $g = \lambda(20+\mathrm{i})$. The numbers beside the curves indicate the value of λ. The attractor is indicated by $\star$. (b) Pole trajectories on $\Sigma'_{\mathrm{II},2}$ obtained when g goes in the g-plane along paths with constant $\mathrm{Im}(g)$ for various values of $\mathrm{Im}(g)$ indicated by the numbers beside the curves. The symbols on each curve indicate the position of the pole for $\mathrm{Re}(g) = 150$ and $\mathrm{Re}(g) = 0$. The bound region of exotic poles is indicated by hatching.

wells (barriers) increases, i. e. there are more bound regions of exotic poles in the same k region when d increases.

Let us analyse the localization of the resonant state wave functions. In order to do this, we introduce the ratios

$$P_1 = \frac{\int_0^a |\psi|^2\,\mathrm{d}x}{\int_0^{d+2a} |\psi|^2\,\mathrm{d}x}, \quad P_2 = \frac{\int_{a+d}^{d+2a} |\psi|^2\,\mathrm{d}x}{\int_0^{d+2a} |\psi|^2\,\mathrm{d}x}. \qquad (15)$$

In Figure 7, the ratios P_1 and P_2 are represented for resonant states (radiative modes) that correspond to the exotic pole situated on the border of the bound region obtained when the potential strength g varies on $\Sigma_{\mathrm{II},1}$ along a path with constant $\mathrm{Im}(g) = \mathrm{Im}(g_{1,1}^{\mathrm{II},1}) + \varepsilon$ and $\mathrm{Re}(g) \geq \mathrm{Re}(g)_{1,1}^{\mathrm{II},1}$. The ratios P_1 and P_2 are almost equal, so that the curves $P_1(g)$ and $P_2(g)$ cannot be distinguished. One can see that $P_1 \ll 1$, $P_2 \ll 1$, on the whole range of $\mathrm{Re}(g)$, i. e. the wave function is mainly localized between the wells. Moreover the minimal localization of the wave function inside the wells occurs for poles near the attractor.

In the following, we shall discuss the range of influence of an attractor for the discussed potential with $d = 4$ and $a = 0.25$. We consider the attractor $\mathcal{K}_1^{\mathrm{II}}$ situated on the Riemann sheet image $\Sigma'_{\mathrm{II},1}$ and calculate the wave functions for several resonant states, corresponding to poles situated in the neighbourhood of $\mathcal{K}_1^{\mathrm{II}}$, or situated away from this attractor. The wave functions are calculated according to (1) with the coefficients A, C_1, ..., C_6, and T determined for each case as a function of k and k_0. The comparison of the wave functions is done after normalizing them by calculating $|\psi(x)|^2 / \int_0^{2a+d} |\psi(x)|^2\,\mathrm{d}x$. The poles denoted $1, 2, \ldots, 6$ on Figure 8c correspond to the potential strengths denoted $1, 2, \ldots, 6$ on Figures 8a and b. The poles 1, 2, and 4 are exotic resonant state poles, while the poles 3, 5, and 6 are old-class poles. The poles 1, 2, 3, and 6 are situated near the attractor $\mathcal{K}_1^{\mathrm{II}} = \pi/2$, while the poles 4 and 5 are situated away from the attractor. The poles 1, 2, 3, 4, and 5 belong to $\Sigma'_{\mathrm{II},1}$, while the pole 6 belongs to $\Sigma'_{\mathrm{II},2}$. In Figure 8d, $|\psi|^2$ is represented for the resonant states corresponding to the poles situated in the neighbourhood of the attractor $\mathcal{K}_1^{\mathrm{II}}$. One can see that for all these poles the corresponding resonant states have the wave function localized mainly in the free region between the two wells. In other words, either we have an exotic resonant state or an usual resonant state, corresponding to a pole situated on the same or another Riemann sheet image, the wave function is localized mainly in the free region between the two wells, provided that the pole is near the attractor. As one can see in Figure 8d, the wave functions of the resonant states corresponding to the poles 1, 2, 3, and 6 are indistinguishable, except for the regions of the two wells. In Figure 8e, the region of the first well is represented at an enlarged scale. In contrast, for poles situated away from the attractor (the poles 4 and 5 on Fig. 8c), the corresponding wave functions have comparable amplitudes inside the wells and between the wells as one can see in Figure 8f.

It is interesting to see the behaviour of the wave functions of the bound states. In Figure 9a, the wave

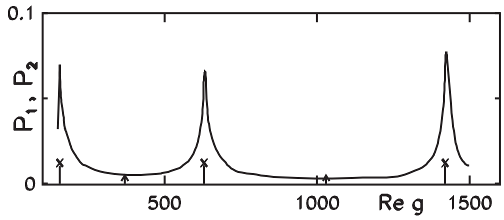

Fig. 7. Ratios P_1 and P_2 for the pole on $\Sigma'_{\mathrm{II},1}$ that correspond to g varying on $\Sigma_{\mathrm{II},1}$ along a path with $\mathrm{Im}(g) = 3.6$ The values of the potential strength for which the pole is at the attractor are indicated by arrows, while by crosses, the values of $\mathrm{Re}(g_{1,\nu}^{\mathrm{II},1})$ are indicated.

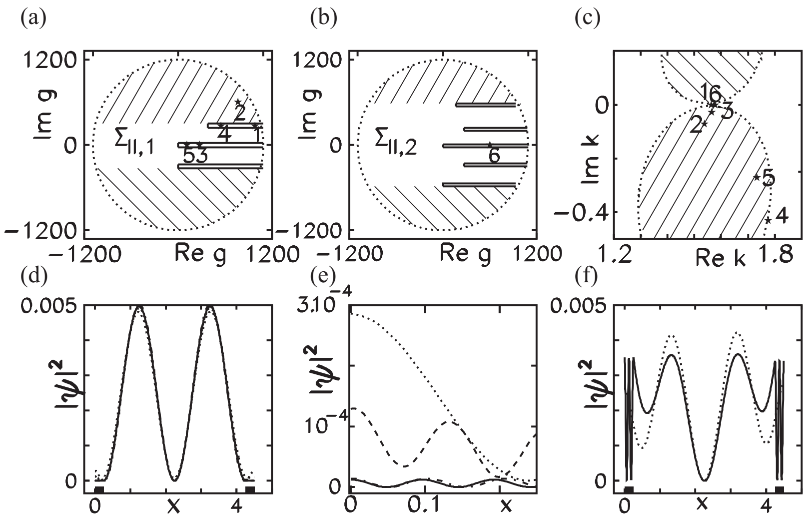

Fig. 8. (a) and (b): Potential strength on $\Sigma_{\mathrm{II},1}$ and on $\Sigma_{\mathrm{II},2}$. (c) Corresponding poles in the k-plane. (d) Wave functions of the resonant states corresponding to the poles situated in the neighbourhood of the attractor $\mathcal{K}_1^{\mathrm{II}}$. The thickened regions of the abscissa indicate the region of the wells. (e) Wave functions from (d) are represented at an enlarged scale in the region of the first well (continuous for Poles 1 and 6, dashed for Pole 2, and dotted for Pole 3). (f) Wave functions of two resonant states corresponding to poles situated away from the attractor (continuous for Pole 4, dotted for Pole 5).

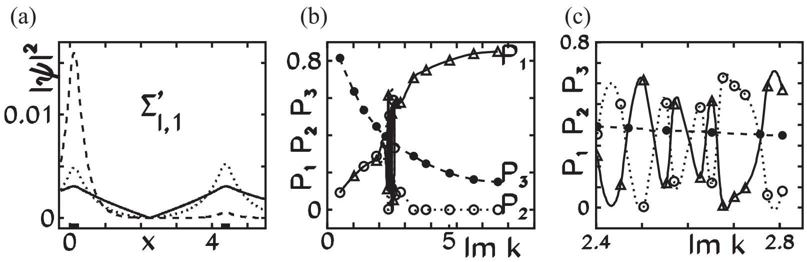

Fig. 9. (a) Wave functions of the bound states on $\Sigma'_{\mathrm{I},1}$ for various binding energies characterized by $k = 0.5\mathrm{i}$ (full line), $k = 1.9\mathrm{i}$ (dotted line), $k = 3.5\mathrm{i}$ (dashed line). (b) Localization of the wave functions corresponding to bound state poles on $\Sigma'_{\mathrm{I},1}$ for various binding energies. (c) Region of (b) where the wave function changes its localization from one well to the other is represented at an enlarged scale. A similar localization of the wave function occurs on $\Sigma'_{\mathrm{II},1}$.

functions of some bound states on $\Sigma'_{\mathrm{I},1}$ and $\Sigma'_{\mathrm{II},1}$ are shown for various binding energies. The thickened regions of the abscissa indicate the regions of the twin wells. For both Riemann sheets $\Sigma'_{\mathrm{I},1}$ and $\Sigma'_{\mathrm{II},1}$, the localization of the wave function of a bound state depends strongly on the energy of the bound state. A quantitative comparison of the localization of the bound state wave functions is done in Figure 9b where the ratios P_1, P_2, and $P_3 = \int_a^{a+d} |\psi|^2\,\mathrm{d}x / \int_0^{d+2a} |\psi|^2\,\mathrm{d}x$, that characterize the localization of the wave function in the first well, in the second well, and in the region between the wells, respectively, are represented as a function of k for bound states from Σ'_I. On Σ'_{II} the situation is identical. At low energies (small k), the ratios P_1 and P_2 are almost equal. Then there is a range of binding energies where the wave function is localized mainly in one or the other of the two wells. This region of energies is shown in more details in Figure 9c. Although the ratios P_1 and P_2 vary strongly with respect to the binding energy in this region, their variations compensate mutually, so that the part of the wave function that is localized between the wells, and characterized by $P_3 = 1 - (P_2 + P_3)$, has a smooth variation with the energy. At higher binding energies, the wave function becomes mainly localized in the first well on both $\Sigma'_{\mathrm{I},1}$ and $\Sigma'_{\mathrm{II},1}$.

6. Traversal Time Through One-Dimensional Twin Square Potentials

The time delay undergone by a particle of mass M during the traversal of the 1D twin square potential is given by the derivative of the phase ϕ of the wave function with respect to energy [14]:

$$\tau = \hbar \frac{\mathrm{d}\phi}{\mathrm{d}E} . \qquad (16)$$

This time delay could be compared to the travel time of a free particle with the same energy on same distance

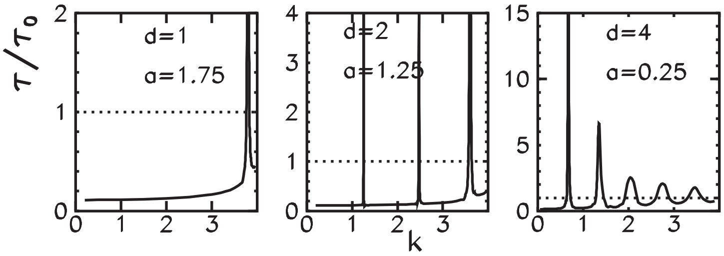

Fig. 10. Dependence of the ratio τ/τ_0 on the wave number k for twin barriers ($g=-16$) and various parameters a and d, with the condition that $2a+d=4.5$.

$(2a+d)$. At $x=0$, the amplitudes of the two waves are both unit, while at $x=2a+d$ they are $\mathrm{e}^{\mathrm{i}k(2a+d)}$ for the free wave and $T(k)\,\mathrm{e}^{\mathrm{i}k(2a+d)}$ for the wave that travels through the potential region. It results that the time taken to the free particle to cover the distance $(2a+d)$ is

$$\tau_0 = \frac{M}{k}(2a+d)\,, \tag{17}$$

while for the particle that travels through the potential region is

$$\tau = \frac{M}{k}\left[(2a+d) + \frac{\mathrm{d}(\mathrm{Im}(\ln T(k)))}{\mathrm{d}k}\right], \tag{18}$$

where $T(k)$ is given by (2). The ratio τ/τ_0 tells us if the wave is delayed or speed up during the potential region traversal as compared to a free wave.

6.1. Twin Barriers

In Figure 10, the ratio τ/τ_0 is represented as a function of the wave number k for various parameters a and d of twin barriers, with the condition that $2a+d$ is the same. Besides the total length of the potential region the height of the barriers is also kept constant ($g=-16$). From the analysis of the results shown in Figure 10 it results that, except for several discrete wave numbers k, situated in the vicinity of the poles of

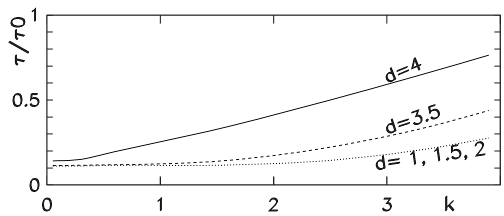

Fig. 11. Ratio τ/τ_0 as a function of k for the same configurations as in Figure 10, but where the resonances have been eliminated.

T for the given configuration, and hence corresponding to resonant states, the traversal time through the twin barriers is less than the time needed to a free wave to travel along the same distance. This is better seen in Figure 11, where the ratio τ/τ_0 is represented as a function of k for various configurations, as in Figure 10, but where the resonances have been eliminated. One can see that the thicker the barriers are the shorter the traversal time is for all frequencies. The difference between the various configurations are larger for k values near the top of the barriers, while for small k values the influence of the barriers is almost the same for all configurations. In the following, the traversal with $\tau > \tau_0$ will be called 'subluminal', while the traversal with $\tau < \tau_0$ will be called 'superluminal', in analogy to the terminology used in the case of electromagnetic waves traversal [25, 26].

In order to tune the experimental conditions for a superluminal or subluminal traversal, it is important to know apriori the potential parameters that determine superluminal or subluminal traversal times. The zeros of the derivative of τ (see (18)) with respect to k, corresponding to maxima and minima of τ/τ_0, respectively, have been calculated and are given in the column 4 of Table 4. An approximate formula would be useful. A first approximation for the frequencies k for which the maxima and minima of τ/τ_0 are obtained are $\frac{n\pi}{d}$, ($n=1,2,\ldots$) for the maxima (k_{sublum}), and $\frac{n\pi}{d}+\frac{\pi}{4d}$ for the minima (k_{suplum}), respectively. In order to obtain a better approximation, the expression of the deviation Δk of π/d with respect to the exact value of k at the first maximum of τ/τ_0 has been obtained as a function of the potential parameters:

$$\Delta k = -\frac{2\pi}{d^3 g}\,\frac{2(\mathrm{e}^{\gamma}+1)^2+\sqrt{-g}\,d(\mathrm{e}^{2\gamma}-1)}{(\mathrm{e}^{\gamma}-1)^2}\,, \tag{19}$$

where $\gamma=-2a\sqrt{-g}$. As a result the following approximate formula for k at the maxima (k_{sublum}) and minima (k_{suplum}) are obtained:

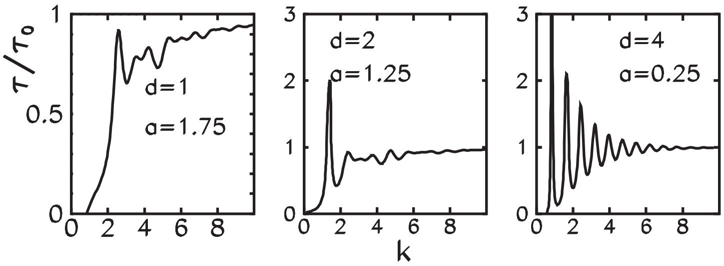

Fig. 12. Dependence of the ratio τ/τ_0 on the wave number k for twin wells with $g = 16$ and various parameters a and d, with the condition that $2a+d = 4.5$.

Table 4. Comparison of approximate and exact frequencies of subluminal and superluminal traversal through twin barriers of constant strength $g = -16$ and different parameters a and d with $2a+d = 4.5$ The quality of the approximations (20) is given by the deviation $\delta = |k_{\text{exact}} - k_{\text{approx}}|/k_{\text{exact}}$.

		$k_{\text{subluminal}}$		
a	d	approx	exact	δ
0.25	4	0.67765	0.67581	0.00271
		1.35530	1.35780	0.00184
		2.03295	2.04934	0.00800
		2.71060	2.75072	0.01459
0.50	3.5	0.78430	0.78121	0.00395
		1.56859	1.55915	0.00605
		2.35289	2.33049	0.00961
		3.13718	3.09203	0.01460
		3.92148	3.84152	0.02081
1.25	2	1.27625	1.25232	0.01911
		2.55251	2.47451	0.03152
		3.82876	3.59915	0.06380
1.5	1.5	1.62897	1.56015	0.04411
		3.25794	3.03853	0.07221
		$k_{\text{superluminal}}$		
a	d	approx	exact	δ
0.25	4	0.87400	0.93403	0.06427
		1.55165	1.65772	0.06399
		2.22930	2.37138	0.05992
		2.90695	3.08705	0.05834
0.50	3.5	1.00870	1.04921	0.0386
		1.79299	1.86524	0.03874
		2.57729	2.64966	0.02731
		3.36158	3.41658	0.01610

$$k_{\text{sublum}} \approx n\left(\frac{\pi}{d} + \Delta k\right), \qquad k_{\text{suplum}} \approx n\left(\frac{\pi}{d} + \Delta k\right) + \frac{\pi}{4d}. \tag{20}$$

The deviation Δk has been calculated for various parameters a and d of the potential, with the condition that $2a+d = 4.5$, and $g = -16$. Although the approximations (20) have been deduced in the condition of large d, one can see that the maxima corresponding to k_{sublum} are rather well approximated even for small d. For small d, the ratio τ/τ_0 depends almost monotonically on k, except for a small number of regions of maxima (subluminal traversal) that could be rather well determined. In this case, if a superluminal traversal is needed, the frequencies for subluminal traversal could be avoided.

6.2. Twin Wells

In Figure 12, the ratio τ/τ_0 is represented as a function of the wave number k for various parameters a and d of twin wells, with the condition that $2a+d$ is the same. Besides the total length of the potential region, the depth of the wells is also kept constant ($g = 16$). One can see that for large k the ratio $\tau/\tau_0 \to 1$ for all configurations, but it is possible to have $\tau/\tau_0 < 1$, in agreement to the results of Li and Wang [27] regarding negative phase time for particles passing through a potential well. Moreover, for small d ($d \leq a$) the ratio $\tau/\tau_0 < 1$ on the whole range of k. For $d > a$, a resonant structure in the dependence of τ/τ_0 on k occurs at small k. The maxima with $\tau > \tau_0$ correspond to exotic resonant states for which the pole k is close to the stable points $\mathcal{K}_n^{\text{I}}$ and $\mathcal{K}_n^{\text{II}}$, given by (14). This is illustrated in Figure 13 for the case $d = 4$, $a = 0.25$, where the resonant structure is the most obvious. The arrows indicate the val-

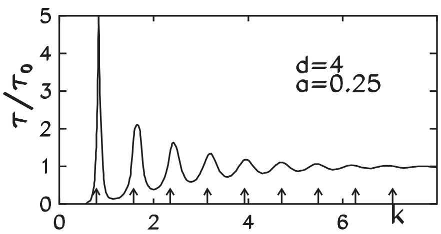

Fig. 13. Dependence of the ratio τ/τ_0 on the wave number k for twin wells with $g = 16$, $a = 0.25$, and $d = 4$. The arrows indicate the values of k for the exotic resonant state poles situated at the stable-points.

ues $k = n\pi/d$, $n = 1,2,3\ldots$, that correspond to both $\mathcal{K}_n^{\mathrm{I}}$ and $\mathcal{K}_n^{\mathrm{II}}$.

7. Conclusions

The natural modes for the twin square potentials of complex strength g are studied by constructing the two Riemann surfaces R_g^{I} and R_g^{II} of the pole function $k(g)$. On the k-plane image of each Riemann sheet there are bound regions where a new class of resonant state poles, with exotic properties, is situated. These exotic poles do not become bound or virtual states when the strength of the potential well is increased, but remain in the neighbourhood of the stable points, that act as attractors. The attractors are situated on the real k-axis, so that the exotic resonant states corresponding to poles in the neighbourhood of the attractors have almost real energies. The density of attractors in the same region of k increases as the distance between the two wells is increased. An exotic resonant state pole in the fourth quadrant of the k-plane occurs for strong absorption of the potential strength, i. e. $\mathrm{Im}(g)$ has to exceed the threshold determined by the imaginary part of the branch point. The exotic resonant states corresponding to poles in the neighbourhood of the attractors have wave functions that are almost completely localized in the free region between the two wells.

The traversal time τ through a one-dimensional twin square potential is compared to the traversal time τ_0 of a free wave. It is shown that for a given configuration of the potential the traversal time through twin barriers is less than the traversal time for a free wave (i. e. there is a 'superluminal' traversal), except for some discrete wave numbers k situated in the neighbourhood of the poles of the transmission coefficient T (i. e. for resonant state poles). In the case of twin wells it is also possible to have $\tau/\tau_0 < 1$, mainly for $d \le a$. The maxima of τ/τ_0 correspond to exotic resonant states for which the pole is situated at an attractor.

[1] G. Nimtz and W. Heitmann, Prog. Quantum Electronics **21**, 81 (1997).
[2] R. Y. Chiao, P. G. Kwiat, and A. M. Steinberg, Physica B: Cond. Matter **175**, 257 (1991).
[3] L. L. Chang, L. Esaki, and R. Tsu, Appl. Phys. Lett. **24**, 593 (1974).
[4] M. T. Björk, B. J. Ohlsson, C. Thelander, A. I. Persson, K. Deppert, L. R. Wallenberg, and L. Samuelson, Appl. Phys. Lett. **81**, 4458 (2002).
[5] C. Thelander, T. Martensson, M. T. Bjrk, B. J. Ohlsson, M. W. Larsson, L. R. Wallenberg, and L. Samuelson, Appl. Phys. Lett. **83**, 2052 (2003).
[6] S. Esposito, Phys. Rev. E **67**, 16609 (2003).
[7] F. Delgado, J. G. Muga, D. G. Austing, and G. Garcia-Calderón, J. Appl. Phys. **97**, 13705 (2005).
[8] M. C. Goorden, Ph. Jacquod, and J. Weiss, Phys. Rev. Lett. **100**, 67001 (2008).
[9] C. Grama, N. Grama, and I. Zamfirescu, Ann. Phys. **218**, 346 (1992).
[10] C. Grama, N. Grama, and I. Zamfirescu, Ann. Phys. **232**, 243 (1994).
[11] C. Grama, N. Grama, and I. Zamfirescu, Phys. Rev. A **61**, 32716 (2000).
[12] S. Collins, D. Lowe and J. R. Barker, J. Phys. C: Solid State Phys. **20**, 6213 (1987).
[13] M. Büttiker, Phys. Rev. B **27**, 6178 (1983).
[14] E. P. Wigner, Phys. Rev. **98**, 145 (1955).
[15] W. E. Hagston, Phys. Status Solidi B **116**, K85 (1983).
[16] F. T. Smith, Phys. Rev. **118**, 349 (1960).
[17] A. Enders and G. Nimtz, Phys. Rev. E **48**, 632 (1993).
[18] T. Hartman, J. Appl. Phys. **33**, 3427 (1962).
[19] G. Nimtz, Prog. Quantum Electronics **27**, 417 (2003).
[20] H. N. Yum, M. Salit, J. Yablon, K. Salit, Y. Wang, and M. S. Shahriar, Optics Express **18**, 17658 (2010).
[21] R. M. Corless, G. H. Gonnet, D. E. G. Hare, D. J. Jeffrey and D. E. Knuth, Adv. Comput. Math. **5**, 329 (1996).
[22] G. Julia, Bull. Soc. Math. France **54**, 26 (1926).
[23] S. Stoilow, Mathematica Cluj **19**, 126 (1943).
[24] S. Stoilow, Leçons sur les Principles Topologiques de la Théory des Fonctions Analitiques, 2nd Ed., Gautier-Villars, Paris 1956.
[25] A. B. Shvartsburg, M. Marklund, G. Brodin, and L. Stenflo, Phys. Rev. E **78**, 16601 (2008).
[26] A. Enders and G. Nimtz, Journal de Physique I **2**, 1693 (1992).
[27] C.-F. Li and Q. Wang, Phys. Lett. A **275**, 287 (2000).